Magnetic Resonance Letters 2 (2022) 147–158

Contents lists available at ScienceDirect

Magnetic Resonance Letters

journal homepage: www.keaipublishing.com/MRL

Research Article

On the use of cross polarization in solid-state NMR: ^{1}H spin-lock versus adiabatic demagnetization in the rotating frame

Dedicated to Professor Chaohui Ye on the occasion of his 80th birthday

Yuchen Li [a, b], Shengyu Zhang [a, b, c], Ze Wu [a, b], Xinhua Peng [a, b, c, *], Riqiang Fu [d, **]

[a] CAS Key Laboratory of Microscale Magnetic Resonance and School of Physical Sciences, University of Science and Technology of China, Hefei, 230026, China
[b] CAS Center for Excellence in Quantum Information and Quantum Physics, University of Science and Technology of China, Hefei, 230026, China
[c] Hefei National Laboratory, Hefei, 230088, China
[d] National High Magnetic Field Laboratory, 1800 East Paul Dirac Drive, Tallahassee, FL, 32310, USA

ARTICLE INFO

Article history:
Received 8 May 2022
Received in revised form 30 June 2022
Accepted 1 July 2022
Available online 15 July 2022

Keywords:
Cross polarization
Spin-lock in rotating frame
Adiabatic demagnetization
Spin dynamics
Dipolar ordered state
Solid-state NMR

ABSTRACT

Cross polarization (CP) is a widely used solid-state nuclear magnetic resonance (NMR) technique for enhancing the polarization of dilute *S* spins from much larger polarization of abundant *I* spins such as ^{1}H. To achieve such a polarization transfer, the *I* spin should either be spin-locked or be converted to the dipolar ordered state through adiabatic demagnetization in the rotating frame. In this work, we analyze the spin dynamics of the Hartmann-Hahn CP (HHCP) utilizing the ^{1}H spin-locking, and the dipolar-order CP (DOCP) having the ^{1}H adiabatic demagnetization. We further propose an adiabatic demagnetization CP (ADCP) where a constant radio-frequency pulse is applied on the *S* spin while ^{1}H is adiabatically demagnetized. Our analyses indicate that ADCP utilizes the adiabatic passage to effectively achieve the polarization transfer from the ^{1}H to *S* spins. In addition, the dipolar ordered state generated during the ^{1}H demagnetization process could also be converted into the observable *S* polarization through DOCP, further enhancing the polarized signals. It is shown by both static and magic-angle-spinning (MAS) NMR experiments that ADCP has dramatically broadened the CP matching condition over the other CP schemes. Various samples have been used to demonstrate the polarization transfer efficiency of this newly proposed ADCP scheme.

1. Introduction

Cross-polarization (CP) [1] has been widely used in solid-state nuclear magnetic resonance (NMR) to enhance the polarization of dilute nuclei *S* with low gyromagnetic ratios (e.g., ^{13}C and ^{15}N) from abundant nuclei *I* with higher gyromagnetic ratios (e.g., ^{1}H). Such a polarization transfer can only take place in the rotating frames where the total energy is conserved. Classically, the *I* spin is either spin-locked in the rotating frame [2] or converted from the Zeeman ordered state to the dipolar

* Corresponding author.
** Corresponding author.
E-mail addresses: xhpeng@ustc.edu.cn (X. Peng), rfu@magnet.fsu.edu (R. Fu).
Peer review under responsibility of Innovation Academy for Precision Measurement Science and Technology (APM), CAS.

https://doi.org/10.1016/j.mrl.2022.07.001

ordered state by adiabatically demagnetizing the *I* magnetization [3,4]. In the former case, the radio-frequency (RF) pulse of the *S* spin is applied during the *I* spin-lock period, such that both *I* and *S* spins are in the so-called doubly rotating frame where the polarization transfer takes place when their RF amplitudes fulfill the Hartmann-Hahn matching condition [2], i.e. $\omega_{1I} = \omega_{1S}$, where $\omega_{1I} = -\gamma_I B_{1I}$ and $\omega_{1S} = -\gamma_S B_{1S}$ are the amplitudes of the RF fields applied to the *I* and *S* spins, respectively. While in the latter case, the RF pulse is applied on the *S* spin after the dipolar ordered state is prepared, such that the thermal contact can be achieved between the dipolar ordered state and the B_{1S} field of the *S* spin in the rotating frame, the so-called dipolar-order CP (DOCP). Therefore, in the Hartmann-Hahn CP (i.e., HHCP) [1], the matching condition must be fulfilled. Since the spin-lock B_1 fields in both spins are applied by the external RF pulses, they are independent of the spin system being investigated. They are subject to the RF inhomogeneities across the sample coil, thus affecting the matching condition, especially when the sample is under fast spinning, where the HHCP matching condition is broken up into a series of sidebands at $\omega_{1I} = \omega_{1S} \pm n\omega_r$ [5,6], here ω_r is the sample spinning rate and *n* is an integer. On the other hand, only the B_{1S} field is applied during the DOCP, thus it should be less sensitive to the RF inhomogeneity as there is no matching condition as in HHCP. However, the local dipolar field highly depends on the spin systems as well as the experimental conditions. For instance, the local dipolar order can hardly be maintained as soon as the sample is spinning, thus the DOCP has never been a choice of the technique especially for rotating solids. Here, we revisit the spin dynamics of CP under ^{1}H spin-locking and adiabatic demagnetization in the rotating frame for spin-1/2 nuclei.

So far, HHCP has been the most popular CP scheme employed in solid-state NMR. Spin dynamics of HHCP has been extensively analyzed [2,7–10]. In general, the polarization buildup for the *S* spin can be characterized by T_{IS} and $T_{1\rho}{}^I$, provided that the spin-lattice relaxation time in the rotating frame for the *S* spin ($T_{1\rho}{}^S$) is long enough that it does not affect the CP spin dynamics. Here, T_{IS} represents the polarization transfer time from the *I* to *S* spins, primarily governed by the strength of the *I*–*S* heteronuclear dipolar coupling and affected by the matching condition [9] and molecular motions [11], while $T_{1\rho}{}^I$ characterizes the *I* spin polarization decay in the rotating frame (or spin-lock) and is highly correlated with spin diffusion, i.e., the homonuclear interactions among the *I* spins. Therefore, broadening the CP matching condition and lengthening $T_{1\rho}{}^I$ are the two primary strategies for maximizing the polarization transfer in the CP experiments when ^{1}H is spin-locked. In the past decades, many spectroscopic approaches have been proposed to enhance the CP efficiency by broadening the matching condition in both static [12–17] and magic-angle-spinning (MAS) [18–27] NMR. While $T_{1\rho}{}^I$ could be lengthened by spin-locking ^{1}H along the magic angle [27], making more effective CP transfer in systems having short $T_{1\rho}{}^I$, such as membrane-bound proteins. While for DOCP, the polarization transfer takes place after ^{1}H is adiabatically demagnetized, which is subject to the lifetime of the dipolar ordered state as characterized by T_{1d}.

In this work, we first analyzed the spin dynamics of HHCP and DOCP using an isolated two-spin system. Different from DOCP where the thermal contact is made only after the dipolar ordered state is prepared, an adiabatic demagnetization CP (ADCP) scheme was proposed where a constant RF pulse is applied on the *S* spin while ^{1}H is adiabatically demagnetized. This ADCP scheme is somehow different from the adiabatic passage through the Hartmann-Hahn cross polarization (APHH-CP) experiments [13,22], where either the *I* and *S* spins are demagnetizing/remagnetizing coordinately, making their total RF amplitude constant, or the *I* spin is spin-locked while the *S* spin is adiabatically passaging through the Hartmann-Hahn condition. Our analyses suggest that, as in APHH-CP, ADCP utilizes the adiabatic passage to effectively achieve the polarization transfer from the *I* to *S* spin. In addition, the dipolar ordered state generated during the ^{1}H demagnetization process could also be converted into the *S* spin, on top of what has been polarized, further enhancing the signals. Furthermore, since ^{1}H is demagnetized, rather than spin-locked, during ADCP, the polarization buildup of the *S* spin is much less prone to the $T_{1\rho}{}^I$ effect. The advantages of the ADCP scheme will be experimentally illustrated under both static and MAS conditions.

2. Theory

Fig. 1 shows the CP schemes to be investigated in this paper. For HHCP, the *I* magnetization after 90° pulse is spin-locked with a constant RF field for a CP contact time of τ_{HHCP}, during which a constant RF is applied on the *S* spin. The polarized signals of the *S* spin are then detected under high-power ^{1}H decoupling. For the ramped-amplitude CP (RACP) [24], the RF amplitude on the *S* spin is ramped during the contact time τ_{RACP} when the ^{1}H is spin-locked, which is commonly used in the MAS experiments to broaden the CP matching condition. For DOCP, the *I* magnetization after 90° pulse is adiabatically demagnetized to the dipolar ordered state, followed by a constant RF irradiation on the *S* spin for a period of τ_{DOCP}. The insertion of a delay τ_d allows for measuring the lifetime of the dipolar ordered state (i.e., T_{1d}). While for ADCP in Fig. 1d, a constant RF field is applied on the *S* spin when the *I* spin is adiabatically demagnetized. At the end of ADCP, the *S* polarization can be further enhanced by the DOCP, i.e., AD/DO-CP, provided that T_{1d} is long, as shown in Fig. 1e.

For the general discussion, we consider an *I*–*S* system with the RF irradiations on both *I* and *S* spins. In a doubly rotating frame synchronized with the Larmor frequencies of ω_{0I} and ω_{0S}, the spin Hamiltonian can be expressed by:

$$H = \Delta\omega_I I_Z + \Delta\omega_S S_Z + \omega_{1I}(t) I_X + \omega_{1S} S_X + 2d_{IS} I_Z S_Z + H_{II}, \quad (1)$$

here, $\Delta\omega_I$ and $\Delta\omega_S$ stand for the resonance offsets for the *I* and *S* spins, respectively, $\omega_{1I}(t)$ represents the time-dependent RF amplitude applied on the *I* spin while ω_{1S} is the constant RF amplitude applied on the *S* spin, and d_{IS} is the heteronuclear dipolar coupling between *I* and *S* spins. H_{II} refers to the homonuclear dipolar interaction among the abundant *I* spins. Because

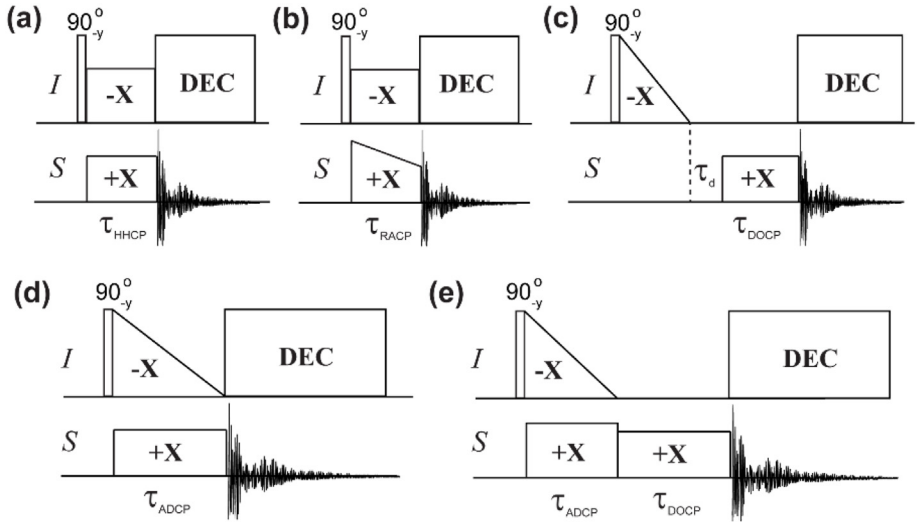

Fig. 1. CP pulse sequences used in our experiments. (a) HHCP; (b) RACP; (c) DOCP; (d) ADCP; and (e) AD/DO-CP.

H_{II} is not directly responsible for polarization transfer between I and S spins, it can be dropped in the following spin operations.

In a doubly tilted interaction frame, the Hamiltonian of Eq. (1) becomes

$$\tilde{H} = \omega_{eI} I_Z + \omega_{eS} S_Z + 2d_{IS} I_X S_X \sin\theta_I \sin\theta_S + 2d_{IS} I_Z S_Z \cos\theta_I \cos\theta_S - 2d_{IS} I_Z S_X \cos\theta_I \sin\theta_S - 2d_{IS} I_X S_Z \sin\theta_I \cos\theta_S - \frac{d\theta_I(t)}{dt} I_Y. \quad (2)$$

Here the effective fields for the I and S spins are $\omega_{eI} = \sqrt{\omega_{1I}^2(t) + \Delta\omega_I^2}$ and $\omega_{eS} = \sqrt{\omega_{1S}^2 + \Delta\omega_S^2}$. The angles $\theta_I(t)$ and θ_S are defined by $\theta_I(t) = \tan^{-1}[\omega_{1I}(t)/\Delta\omega_I]$ and $\theta_S = \tan^{-1}[\omega_{1S}/\Delta\omega_S]$.

Assuming on-resonance irradiations on both I and S spins, we have $\theta_I(t) = \theta_S = 90°$, so that Eq. (2) can be simplified as:

$$\tilde{H} = \omega_{1I}(t) I_Z + \omega_{1S} S_Z + 2d_{IS} I_X S_X. \quad (3)$$

By defining the single-transition operators, i.e., $I_Z^\Delta = (I_Z - S_Z)/2$, $I_X^\Delta = I_X S_X + I_Y S_Y$, and $I_Y^\Delta = I_Y S_X - I_X S_Y$ in the zero-quantum subspace and $I_Z^\Sigma = (I_Z + S_Z)/2$, $I_X^\Sigma = I_X S_X - I_Y S_Y$, and $I_Y^\Sigma = I_X S_Y + I_Y S_X$ in the double-quantum subspace, we have

$$\tilde{H} = \tilde{H^\Delta} + \tilde{H^\Sigma}. \quad (4)$$

With the definition of $\Delta(t) = \omega_{1I}(t) - \omega_{1S}$ and $\Sigma(t) = \omega_{1I}(t) + \omega_{1S}$, we have

$$\tilde{H^\Delta} = \Delta(t) I_Z^\Delta + d_{IS} I_X^\Delta, \quad (5)$$

$$\tilde{H^\Sigma} = \Sigma(t) I_Z^\Sigma + d_{IS} I_X^\Sigma. \quad (6)$$

Since the zero- and double-quantum subspaces are commuted with each other, the Hamiltonians in these two subspaces, as diagramed in Fig. 2, can be treated separately. Both subspaces represent the inter-conversion between the Zeeman order (I_Z^Δ and I_Z^Σ) and the dipolar order (I_X^Δ and I_X^Σ).

Let's consider different CP schemes shown in Fig. 1. In the case of HHCP (c.f., Fig. 1a) where the constant RF amplitudes are applied simultaneously, the initial density matrix is

$$\widetilde{\rho(0)} = \widetilde{\rho^\Delta(0)} + \widetilde{\rho^\Sigma(0)}, \quad (7)$$

where $\widetilde{\rho^\Delta(0)} = \frac{I_Z - S_Z}{2} = I_Z^\Delta$ and $\widetilde{\rho^\Sigma(0)} = \frac{I_Z + S_Z}{2} = I_Z^\Sigma$.

As indicated in red in Fig. 2, the initial density matrix $\widetilde{\rho^\Delta(0)}$ and $\widetilde{\rho^\Sigma(0)}$ are rotated under $\tilde{H^\Delta}$ and $\tilde{H^\Sigma}$ in the zero- and double-quantum subspaces, respectively. When $\Delta < d_{IS}$, the cross polarization takes place in the zero-quantum subspace and the most efficient transfer occurs at $\Delta = 0$ (i.e., $\omega_{1I} = \omega_{1S}$), the so-called Hartmann-Hahn matching condition, when the direction of the effective Hamiltonian is along I_X^Δ. While in the double-quantum subspace, the condition of $\Sigma \gg d_{IS}$ is easily fulfilled with the

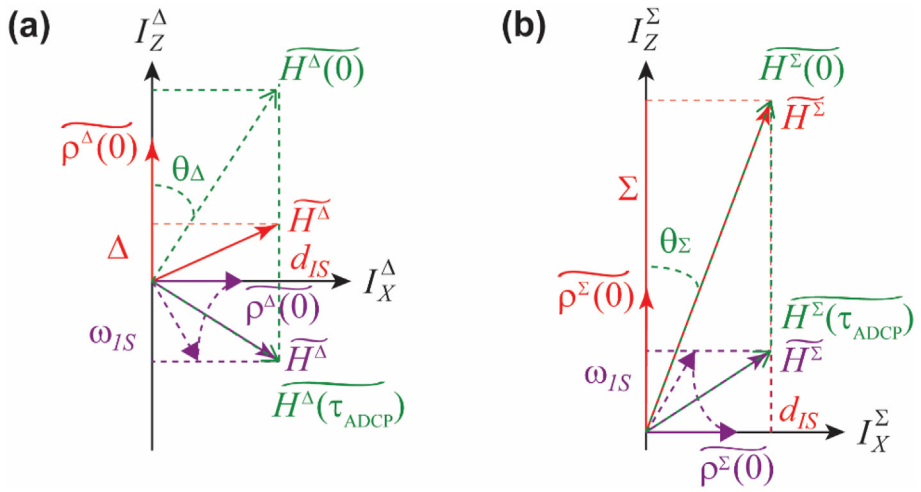

Fig. 2. Schematic representations of Hamiltonians in (a) the zero-quantum subspace and (b) double-quantum subspace. The effective fields and initial density matrix in the HHCP, DOCP, and ADCP schemes are represented in red, purple, and green, respectively.

strong RF fields. As a result, $\widetilde{\rho^\Sigma(0)}$ does not evolve under the Hamiltonian and thus no cross polarization takes place in the double-quantum subspace.

In the case of DOCP in Fig. 1c, the RF pulse is applied only on the I spin during the adiabatic demagnetization period, so that $\omega_{1S} = 0$, i.e., $\Sigma = \Delta$. At the end of the adiabatic demagnetization period, the dipolar order $I_X S_X$ is prepared before DOCP. Therefore, the initial spin density matrix in the zero- and double-quantum subspaces are $\widetilde{\rho^\Delta(0)} = \frac{I_X S_X + I_Y S_Y}{2} = \frac{1}{2} I_X^\Delta$ and $\widetilde{\rho^\Sigma(0)} = \frac{I_X S_X - I_Y S_Y}{2} = \frac{1}{2} I_X^\Sigma$. Since no RF amplitude is applied on the I spin, the dipolar orders in both subspaces could be evolved into the z-axis as long as an RF amplitude is applied on the S spin making their effective fields away from the x-axis. As indicated in Fig. 2, since $\omega_{1I} = 0$, thus $\Sigma = \omega_{1S} = -\Delta$, the initial spin density of the dipolar ordered state $\widetilde{\rho^\Delta(0)}$ is projected into the (-z)-axis under the Hamiltonian $\tilde{H}^\Delta$ in the zero-quantum subspace (the rotation in purple), i.e., converted into $+S_Z$, while the initial spin density of the dipolar ordered state $\widetilde{\rho^\Sigma(0)}$ is projected into the (+z)-axis under the Hamiltonian $\tilde{H}^\Sigma$ in the double-quantum subspace (the rotation in purple), i.e., converted into $+S_Z$ as well. According to these schematic diagrams in Fig. 2, the most efficient conversion from the dipolar order into the S polarization in DOCP takes place when $\omega_{1S} = d_{IS}$ in both subspaces.

On the other hand, in the case of ADCP in Fig. 1d, the RF amplitude on the I spin is linearly decreased to zero while that on the S spin remains constant. As in HHCP, the initial spin density matrix in the zero- and double-quantum subspaces are $\widetilde{\rho^\Delta(0)} = \frac{I_Z - S_Z}{2} = I_Z^\Delta$ and $\widetilde{\rho^\Sigma(0)} = \frac{I_Z + S_Z}{2} = I_Z^\Sigma$, respectively. However, the effective Hamiltonians in both subspaces become time-dependent, as indicated by green dashed lines in Fig. 2. The titled angles $\theta_\Delta(t)$ and $\theta_\Sigma(t)$ are defined as $\theta_\Delta = \tan^{-1}[d_{IS}/\Delta(t)]$ and $\theta_\Sigma = \tan^{-1}[d_{IS}/\Sigma(t)]$. Because ω_{1I} is linearly decreased from its maximum ω_{1I}^{max} to zero during the contact time τ_{ADCP}, the derivative of these tilted angles can be obtained as:

$$\frac{d\theta_\varepsilon(t)}{dt} = \frac{d_{IS}\omega_{1I}^{max}}{\left(\omega_{eff}^\varepsilon\right)^2 \tau_{ADCP}}. \tag{8}$$

Here, $\varepsilon = \Delta$ or Σ. The effective field ω_{eff}^ε is defined as $\omega_{eff}^\varepsilon = \sqrt{d_{IS}^2 + \varepsilon^2(t)}$. When $\left|\frac{d\theta_\varepsilon(t)}{dt}\right| \ll \omega_{eff}^\varepsilon$, the adiabatic condition is fulfilled, meaning that the initial density matrix $\widetilde{\rho^\Delta(0)}$ and $\widetilde{\rho^\Sigma(0)}$ follow the directions of the effective fields in their respective subspaces. Thus, in the zero-quantum subspace, because $\widetilde{\rho^\Delta(0)}$ follows the direction of the effective field $\tilde{H}^\Delta$, the projection onto the z-axis is $\widetilde{\rho^\Delta(t)} = \widetilde{\rho^\Delta(0)}\cos(\theta_\Delta(t)) = \frac{I_Z - S_Z}{2}\left(\frac{\Delta}{\omega_{eff}^\Delta}\right)$. When $\Delta = 0$ (i.e., $\omega_{1I} = \omega_{1S}$), the effective field is crossing the x-axis and thus it is expected to have maximal slope of the polarization transfer. At the end of τ_{ADCP} where $\omega_{1I} = 0$ and $\Delta = -\omega_{1S}$, the projection onto the z-axis becomes $\rho^\Delta(\widetilde{\tau_{ADCP}}) = \frac{I_Z - S_Z}{2}\left(\frac{-\omega_{1S}}{\sqrt{\omega_{1S}^2 + d_{IS}^2}}\right)$. Similarly, in the double-quantum subspace, as $\widetilde{\rho^\Sigma(0)}$ follows the direction of the effective field $\tilde{H}^\Sigma$, the projection onto the z-axis is $\widetilde{\rho^\Sigma(t)} = \widetilde{\rho^\Sigma(0)}\cos(\theta_\Sigma(t)) = \frac{I_Z + S_Z}{2}\left(\frac{\Sigma}{\omega_{eff}^\Sigma}\right)$. However, because the condition of $\Sigma \gg d_{IS}$ is easily fulfilled with the strong RF fields at the beginning of the ADCP contact, the effective field has such little change that $\widetilde{\rho^\Sigma(0)}$ remains almost stationary. With the further decrease in ω_{1I}, the effective field starts to

move along the vertical green dashed line and eventually coincides with the purple $\tilde{H^{\Sigma}}$, i.e., the green $H^{\Sigma}(\widetilde{\tau_{ADCP}})$, at the end of τ_{ADCP} where $\omega_{1I} = 0$ and $\Sigma = \omega_{1S}$, thus the projection onto the z-axis becomes $\rho^{\Sigma}(\widetilde{\tau_{ADCP}}) = \frac{I_Z+S_Z}{2}\left(\frac{\omega_{1S}}{\sqrt{\omega_{1S}^2+d_{IS}^2}}\right)$. The evolution of the initial density matrix $\widetilde{\rho(0)} = I_Z$ (in Eq. (7)) projected onto the z-axis during τ_{ADCP} can be described as

$$\widetilde{\rho(t)} = \widetilde{\rho^{\Delta}(t)} + \widetilde{\rho^{\Sigma}(t)} = \frac{I_Z - S_Z}{2}\left(\frac{\Delta}{\omega_{eff}^{\Delta}}\right) + \frac{I_Z + S_Z}{2}\left(\frac{\Sigma}{\omega_{eff}^{\Sigma}}\right) = C_I(t)I_Z + C_S(t)S_Z. \quad (9)$$

Here, $C_I(t) = 0.5\left(\frac{\Delta}{\omega_{eff}^{\Delta}} + \frac{\Sigma}{\omega_{eff}^{\Sigma}}\right)$ and $C_S(t) = 0.5\left(\frac{-\Delta}{\omega_{eff}^{\Delta}} + \frac{\Sigma}{\omega_{eff}^{\Sigma}}\right)$ represent the remaining I polarization and the polarized S spin, respectively. At the end of τ_{ADCP} where $\omega_{1I} = 0$, $\Sigma = \omega_{1S}$, and $\Delta = -\omega_{1S}$, we have $C_I(\tau_{ADCP}) = 0$ and $C_S(\tau_{ADCP}) = \frac{\omega_{1S}}{\sqrt{\omega_{1S}^2+d_{IS}^2}}$, implying that I_Z is completely transferred into S_Z, with a scaling factor of $\frac{\omega_{1S}}{\sqrt{\omega_{1S}^2+d_{IS}^2}}$. Fig. S1 shows the plot of $C_I(t)$ and $C_S(t)$ at different ω_{1S}. Importantly, the effective fields in both subspaces have projection onto their x-axis, suggesting that the dipolar ordered states are generated in both subspaces, which could be adopted for additional polarization transfer using DOCP, as shown in Fig. 1e where DOCP is followed right after ADCP. It is worth noting that, although $I_Z^{\Delta} = (I_Z - S_Z)/2$ and $I_Z^{\Sigma} = (I_Z + S_Z)/2$ are defined in the zero- and double-quantum subspace, respectively, the total initial density matrix (i.e., the sum of them from both subspaces) does not contain any S_Z component, indicating that any existing S polarization will not be converted into the dipolar order. In other word, DOCP does not affect any existing S_Z polarization before the contact time, but to add additional polarization during the DOCP contact time by converting the dipolar ordered state into the S_Z polarization, allowing for further increasing the sensitivity, provided that the lifetime of the dipolar ordered state is long enough.

3. Experimental

All NMR experiments were carried out on a mid-bore 800 MHz NMR spectrometer equipped with a Bruker NEO console where the ^{15}N and ^{13}C Larmor frequencies are 81.1 and 201.1 MHz, respectively. For the static ^{15}N measurements, a home-made low electrical field ^{1}H–^{15}N double-resonance probe with a rectangular coil dimension of 7.6 mm * 5.6 mm* 11 mm was used. Since both ^{1}H and broadband amplifiers were linearized through the Cortab procedures for the NEO console, the RF amplitude at any RF power can be calculated from the calibrated RF amplitude at a given RF power. Experimentally, the ^{1}H RF amplitude of 62.5 kHz (i.e., 4 μs 90° pulse length) was calibrated at 260 Watts power and the ^{15}N RF amplitude of 50.0 kHz (i.e., 5 μs 90° pulse length) at 530 Watts power. Thus, the ^{1}H RF power of 166 Watts gave rise to the RF amplitude of 50.0 kHz (i.e., 5 μs 90° pulse length) according to this formula of $62.5*\sqrt{(166/260)}$ kHz, which was experimentally verified. During the ^{15}N acquisition, the phase-wiggled two-pulse phase modulation scheme [28] was used for decoupling with a ^{1}H RF amplitude of 62.5 kHz. The ^{15}N chemical shifts were externally referenced to the ^{15}N signal of the NH_4Cl powder at 39.3 ppm.

The ^{13}C MAS experiments were conducted using a home-made low electrical field 3.2 mm MAS NMR probe. The sample of natural abundance alanine amino acid, purchased from Cambridge Isotope Laboratories, Inc. and used without further purification, was spun at 17 kHz ±5 Hz. The ^{1}H RF amplitude of 50 kHz (i.e., 5.0 μs 90° pulse length) was calibrated at the RF power of 81.9 Watts and the ^{13}C RF amplitude of 62.5 kHz (i.e., 4.0 μs 90° pulse length) at the RF power of 110 Watts. In all MAS experiments, 16 scans were applied to accumulate the ^{13}C signals with a recycle delay of 10 s. During ^{13}C acquisition, the SPINAL sequence [29] was used for ^{1}H decoupling with an RF amplitude of 62.5 kHz.

4. Results and discussion

Fig. 3 shows the ^{15}N spectra of ^{15}N-acetyl-valine (NAV) crystals at an arbitrary orientation using various CP schemes shown in Fig. 1. At this orientation, four groups of resonances were observed at ~200, ~170, 45, and 40 ppm, due to the magnetically inequivalent sites in the unit cell. To generate the 50 kHz spin-lock fields, 530 and 166 Watts were used with such a large rectangular coil (7.6 mm * 5.6 mm* 11 mm) in the ^{15}N and ^{1}H channels, respectively, in the HHCP experiments. Especially for low gamma nuclei such as ^{15}N, further increasing the RF amplitude becomes practically difficult. While in the DOCP experiments the ^{15}N RF power used was considerably lower. Compared to the HHCP spectrum, the resulting DOCP spectrum has slightly higher signal intensities at ~170 and 40 ppm, enhanced by 10% and 18%, respectively, but lower signal intensities at ~200 and 45 ppm, reduced by 25% and 7% respectively. Since the polarization buildup in the DOCP experiments is highly dependent upon the applied ^{15}N RF amplitude and offset (*vide infra*), it would be very difficult to have the optimal polarization enhancement for all resonances in the entire spectral window.

Noticeably in Fig. 3, the ADCP experiments not only used a considerably lower ^{15}N RF power (200 Watts in ADCP versus 530 W in HHCP) but also resulted in better enhancement for all resonances, as compared to the HHCP experiments. For the signals at ~200, ~170, 45 and 40 ppm, their intensities were enhanced by 30%, 30%, 6%, and 18%, respectively. When the DOCP is applied right after the ADCP, the AD/DO-CP experiments further extend their respective enhancement to 35%, 47%, 41%, and 55%.

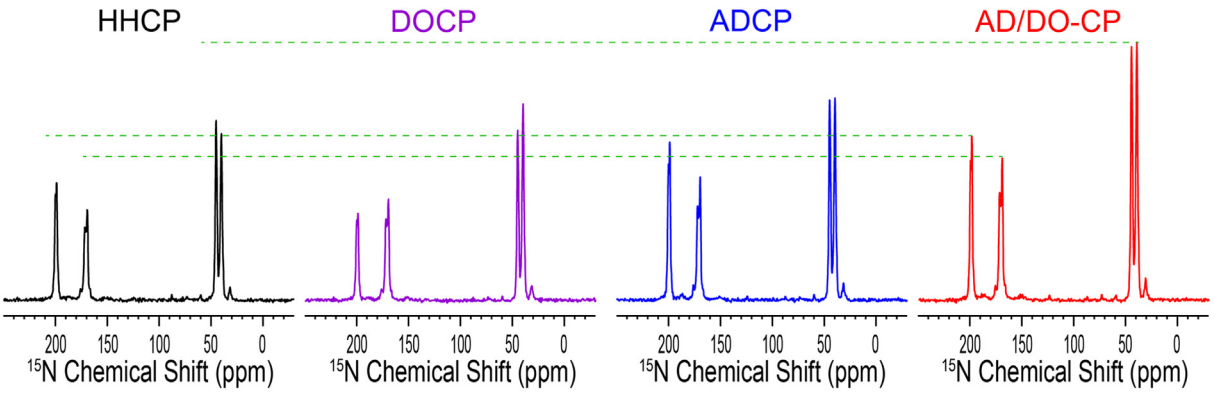

Fig. 3. ^{15}N spectra of static NAV crystals observed using various CP schemes shown in Fig. 1. For HHCP: τ_{HHCP} = 2 ms, ω_{1H} = 50.0 kHz (at 166 Watts), ω_{1N} = 50.0 kHz (at 530 Watts). For DOCP, 2 ms was used for adiabatic demagnetization from 62.5 kHz to 0, τ_d = 0, and τ_{DOCP} = 10 ms, and ω_{1N} = 19.4 kHz (at 80 Watts). For ADCP, τ_{ADCP} = 2 ms was used for adiabatic demagnetization from 62.5 kHz to 0 and ω_{1N} = 30.7 kHz (at 200 Watts). For AD/DO-CP, the same experimental conditions as in the ADCP and DOCP experiments were used. The green dashed lines are used to guide their relative signal intensities.

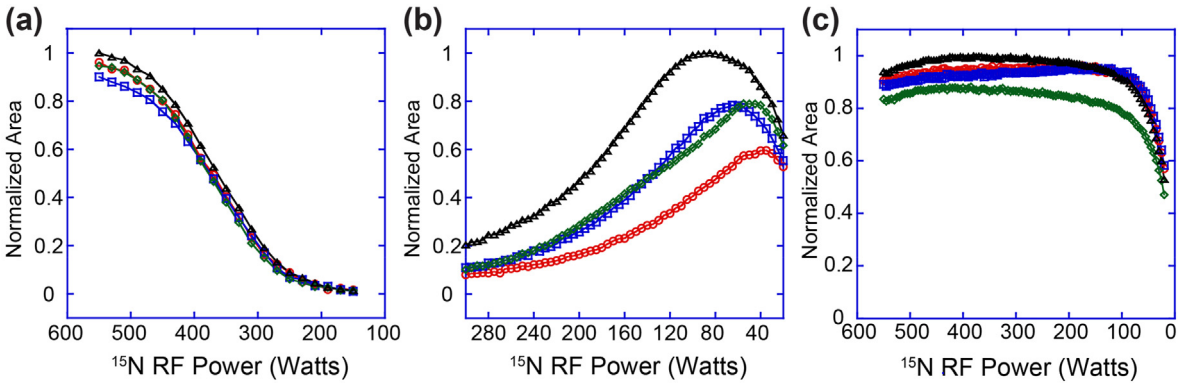

Fig. 4. The observed ^{15}N intensities of static NAV crystals as a function of the applied ^{15}N RF power with the three different CP schemes. (a) HHCP where the ^{1}H RF power of 166 Watts is applied throughout τ_{HHCP} = 2 ms. (b) DOCP where various ^{15}N RF power is applied to the resonance at 40 ppm after the ^{1}H is adiabatically demagnetized from 62.5 kHz to 0, with τ_d = 0 and τ_{DOCP} = 10 ms. (c) ADCP where the ^{1}H is adiabatically demagnetized from 62.5 kHz to 0 in τ_{ADCP} = 2 ms. In these matching profiles, the integral signals at ~200, ~170, 45, and 40 ppm are indicated by the circles (red), squares (blue), diamond (green) and triangles (black), respectively.

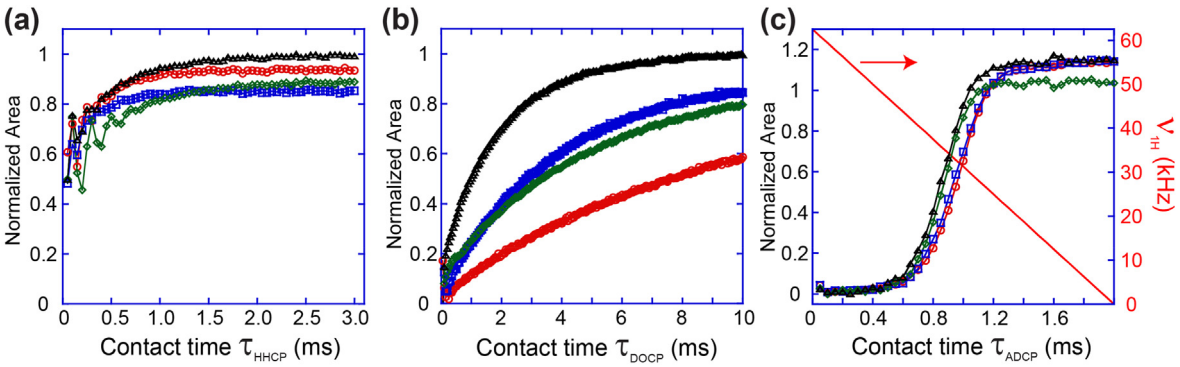

Fig. 5. Buildups of the observed ^{15}N signals of static NAV crystals during the contact time in different CP schemes. (a) HHCP where the RF powers of 166 and 530 Watts were applied on ^{1}H and ^{15}N, respectively. (b) DOCP where the ^{15}N RF power of 80 Watts is applied to the resonance at 40 ppm after the ^{1}H is adiabatically demagnetized from 62.5 kHz to 0. (c) ADCP where the ^{1}H is adiabatically demagnetized from 62.5 kHz to 0 and the ^{15}N RF power of 200 Watts (ω_{1N} = 30.7 kHz) is used. The right vertical scale in red shows the transient ^{1}H RF amplitude during the contact time. In these matching profiles, the signals at ~200, ~170, 45, and 40 ppm are indicated by the circles (red), squares (blue), diamond (green) and triangles (black), respectively.

Fig. 4 shows the CP matching profiles, i.e., the plots of the observed ^{15}N intensities as a function of the applied ^{15}N RF power in the three different CP schemes. For the safety of the probe, the maximum ^{15}N RF power was limited to 550 Watts, corresponding to $\omega_{1N} = 50.9$ kHz. For HHCP, all ^{15}N intensities behaved in the same way by being maximal at the power of 550 Watts but reduced to ~50% when the RF power was deviated by 32% to 370 Watts, corresponding to $\omega_{1N} = 41.8$ kHz. However, for DOCP, the matching profile is highly dependent upon the ^{15}N irradiation position. As indicated in Fig. 4b where the ^{15}N irradiation was applied to the position at 40 ppm, the ^{15}N signals at 40, 45, ~170, and ~200 ppm reached their maximum at 90 (i.e., $\omega_{1N} = 20.6$ kHz), 50 (i.e., $\omega_{1N} = 15.4$ kHz), 70 (i.e., $\omega_{1N} = 18.2$ kHz), and 40 (i.e., $\omega_{1N} = 13.7$ kHz) Watts, respectively, with the signals at ~200 ppm much less than the others. As shown in Fig. S2a, when the ^{15}N irradiation was applied to the position at 185 ppm, the ^{15}N signals at 40, 45, ~170, and ~200 ppm reached their maximum plateau at 65 (i.e., $\omega_{1N} = 17.5$ kHz), 40 (i.e., $\omega_{1N} = 13.7$ kHz), 100 (i.e., $\omega_{1N} = 21.7$ kHz), and 80 (i.e., $\omega_{1N} = 19.4$ kHz) Watts, respectively, with much improved signal intensities at ~200 and ~170 ppm. Clearly, the ^{15}N RF amplitudes used for the maximum polarization in the DOCP experiments are much less than that in the HHCP experiments and the matching bandwidths in terms of the RF power deviation are much larger (over 100% in DOCP versus 32% in HHCP). It was estimated that the ^{1}H–^{15}N dipolar couplings were ~10 kHz at this orientation, while the ^{15}N RF amplitudes for the maximum polarization in the DOCP experiments were in the range between 13.7 and 21.7 kHz, which is roughly about twice of the ^{1}H–^{15}N dipolar couplings. As projected in Fig. 2, the most efficient conversion from the dipolar order into the *S* polarization in DOCP takes place when $\omega_{1S} = d_{IS}$ in the zero- and double-quantum subspaces. Since ω_{1S} in the zero- and double-quantum subspaces is only half of what it is in the rotating frame, these experimental observations presented here agree with the theoretical predictions. As for ADCP, all ^{15}N intensities are almost flat over the ^{15}N RF power from 550 to 100 Watts, only starting to decrease below 100 Watts and reduce at ~50% at 20 Watts, as shown in Fig. 4c. In another word, the matching profiles cover the entire range of the ^{15}N RF power used in the experiments.

To study the "buildup" behavior, we have examined the ^{15}N signal intensities during the CP contact time, as shown in Fig. 5. For HHCP, the matching condition of $\omega_{1N} = \omega_{1H} = 50$ kHz was used. As clearly indicated in Fig. 5a, the ^{15}N signal intensities increase with oscillations at the beginning and reach their respective plateau when τ_{HHCP} is ~2 ms. For DOCP, when the ^{15}N irradiation was applied to the position at 40 ppm, the ^{15}N signal intensities also appear to have some degree of oscillation at the beginning of the contact time and then increase rather slowly, as compared to that in the HHCP experiments. As clearly illustrated in Fig. 5b, the signal at 40 ppm evidently builds up much faster than the other signals. When the ^{15}N irradiation was applied to the position at 185 ppm, the intensities buildups for the resonances at ~200 and ~170 ppm become much faster than those at 45 and 40 ppm (c.f., Fig. S2b). In addition, a lower RF amplitude in DOCP also increases the signal buildups (c.f., Fig. S2c). It has been rationalized [9] that the polarization buildup in DOCP is highly correlated with the effective field applied on the *S* spin, which depends on the irradiation offset and the RF amplitude. The less effective field results in the faster polarization buildup. Unfortunately, the weaker RF amplitude used in DOCP could also result in a smaller achievable polarization as shown in the matching profiles of Fig. 4b.

Another consideration in the DOCP experiments is the lifetime of the dipolar ordered state, which depends highly on the systems being investigated. Fig. S3 shows the DOCP enhanced signal intensities as a function of τ_d. The fittings with a single exponential decay yielded the T_{1d} values of 412 ± 5, 425 ± 6, 398 ± 12, and 417 ± 8 ms for the resonances at ~200, ~170, 45, and 40 ppm, respectively. In other words, the local dipolar order could last hundreds of milliseconds for ^{15}N in the NAV crystals, enabling us to acquire the signals multiple times as long as the dipolar ordered state can be maintained. However, for peptides in hydrated lipids, the T_{1d} values tend to be very short (*vide infra*), making it practically impossible to enhance the signals through DOCP.

On the other hand, the signal intensities buildups appear to be very different in the ADCP experiments. As shown in Fig. 5c, the ^{15}N signals could not be observed when $\tau_{ADCP} < 0.5$ ms, and then rapidly increase without any oscillation when τ_{ADCP} is between 0.7 and 1.2 ms (faster than in the HHCP experiments), and then continue to increase slowly until the end of the CP

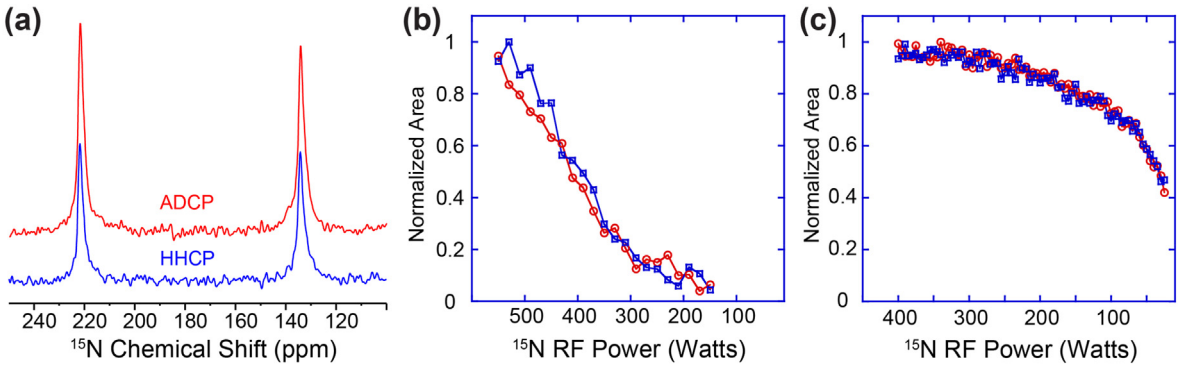

Fig. 6. (a) ^{15}N signals of ^{15}N-Gly$_2$, ^{15}N-Ala$_3$ gA mechanically aligned in hydrated dimyristoylphosphatidylcholine (DMPC) recorded using HHCP (blue) and ADCP (red). For HHCP, the RF powers of 166 and 530 Watts were used on ^{1}H and ^{15}N, respectively, and $\tau_{HHCP} = 1$ ms. For ADCP, the ^{1}H was linearly decreased from 62.5 kHz to 0, the ^{15}N RF power of 350 Watts ($\omega_{1N} = 40.6$ kHz) was used, and $\tau_{ADCP} = 1$ ms. Using these ^{1}H conditions, the matching profiles, i.e., the ^{15}N intensities as a function of the applied ^{15}N RF power, are plotted in (b) for HHCP and (c) for ADCP. In these matching profiles, the ^{15}N-Gly$_2$ signal at 136 ppm and ^{15}N-Ala$_3$ signal at 222 ppm are indicated by squares (blue) and circles (red), respectively.

contact. Similar buildup curves were observed with different ^{15}N RF powers, as shown in Fig. S4, except that the maximum slope of the polarization buildups appears at the position where the transient ^{1}H RF amplitude is coincided with the applied ^{15}N RF amplitude, i.e., $\omega_{1N} \sim \omega_{1H}$ or $\Delta \sim 0$. For instance, in Fig. 5c where the ^{15}N RF power of 200 Watts was used, corresponding to $\omega_{1N} = 30.7$ kHz, the maximum slope of the polarization buildups was observed at $\tau_{ADCP} = 1$ ms when the transient ω_{1H} was passing through 31 kHz. Similarly, when the ^{15}N RF power of 425 Watts was used (i.e., $\omega_{1N} = 44.8$ kHz), the most effective polarization transfer rate took place at $\tau_{ADCP} = 0.55$ ms (c.f., Fig. S4a) when the transient ω_{1H} was passing through 45.0 kHz. While at $\omega_{1N} = 21.7$ kHz (c.f., Fig. S4b), the transient ω_{1H} was passing through 22.0 kHz at $\tau_{ADCP} \sim 1.20$ ms, where the polarization transfer rate was maximal. These observations agree well with the theoretical analysis as shown in Fig. S1, implying that the adiabatic conditions were fulfilled in these experimental setups.

Therefore, since ω_{1H} is adiabatically decreased (in our case, it is linearly reduced to zero), a large range of ω_{1N} can fulfill the matching condition of $\Delta = 0$ at different positions during τ_{ADCP}. As a result, the matching bandwidth becomes extremely broad as indicated in Fig. 4c. We further confirm that the dipolar ordered state generated at the end of τ_{ADCP} can be used for additional enhancement (c.f., Fig. 3). As shown in Fig. S5, the ^{15}N signals increase further with DOCP, especially for the resonances at 45 and 40 ppm, since a weaker ^{15}N RF power of 80 Watts was applied to the position at 40 ppm during DOCP.

Because the polarization transfer in the DOCP experiments is rather slow as compared to that in the HHCP and ADCP experiments, it is prerequisite to have a long enough T_{1d} for maximizing the polarization transfer. However, for membrane proteins/peptides oriented in hydrated phospholipid bilayers, from which orientational restraints of anisotropic nuclear spin

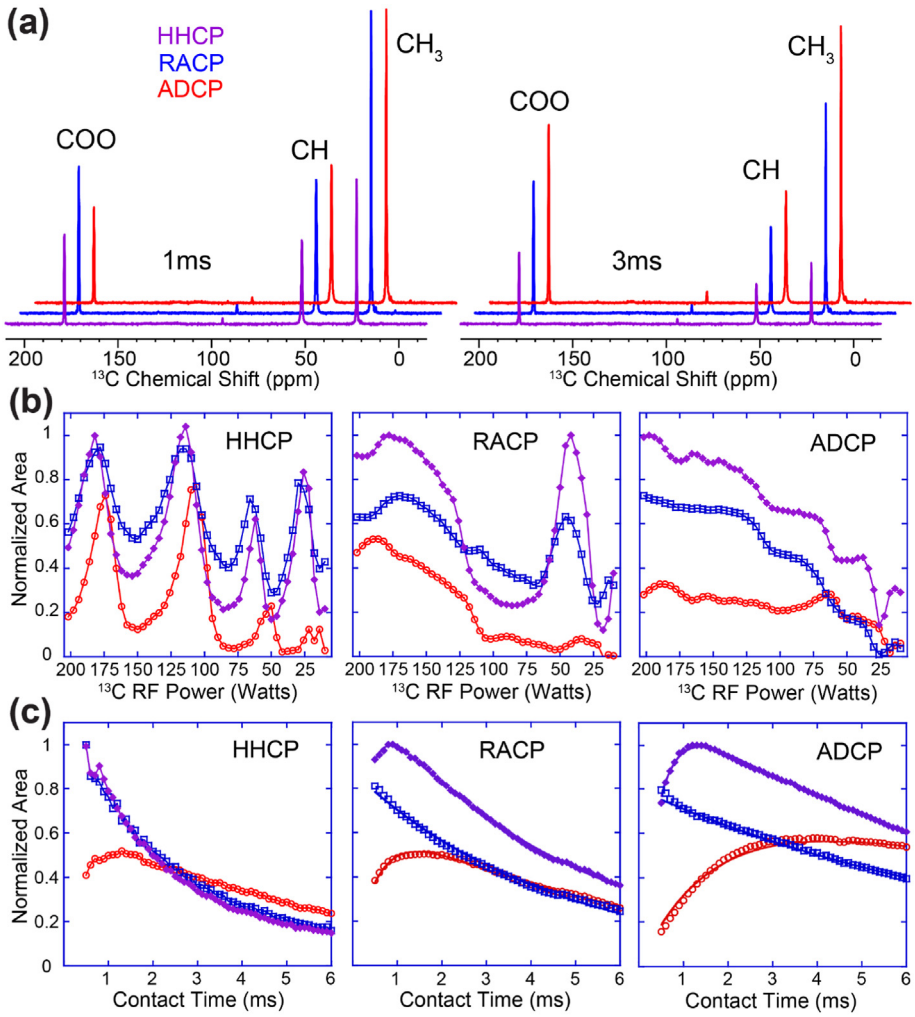

Fig. 7. (a) The normalized ^{13}C CPMAS spectra of the alanine powder sample spinning at 17 kHz using HHCP, RACP, and ADCP at the contact time of 1 (left) and 3 (right) ms. (b) ^{13}C intensities as a function of the applied ^{13}C RF power. In the HHCP and RACP experiments, the ^{1}H RF power of 81.9 Watts (i.e., $\omega_{1H} = 50$ kHz) was used with a CP contact time of 1 ms, while in the ADCP experiments, the ^{1}H RF amplitude was linearly ramped down from 78 (i.e., 200 Watts) to 0 kHz in 1 ms. (c) Buildups of the ^{13}C signals as a function of contact time in different CP schemes. The ^{13}C RF power was set to 182, 178 (maximum), and 198 Watts, respectively in the HHCP, RACP, and ADCP experiments. In (b) and (c), the COO, CH, and CH_3 signals are indicated by the circles (red), squares (blue), and solid diamonds (purple), respectively.

Table 1
$T_{1\rho}{}^{H}$ and T_{CH} values obtained from variable contact RACP and ADCP experiments.

	RACP		ADCP	
	$T_{1\rho}{}^{H}$ (ms)	T_{CH} (ms)	$T_{1\rho}{}^{H}$ (ms)	T_{CH} (ms)
CH_3	4.74 ± 0.01	0.28 ± 0.01	8.62 ± 0.09	0.43 ± 0.01
CH	4.56 ± 0.04	n/a	8.74 ± 0.12	n/a
COO	6.12 ± 0.10	0.54 ± 0.01	17.32 ± 4.52	1.63 ± 0.14

interactions can be used for structural elucidations in their native-like environment, the lifetime of the dipolar ordered states appears to be short, probably due to the presence of a significant degree of dynamics associated with the hydrated lipids. As an example, Fig. 6a shows the ^{15}N spectra of a mechanically (with glass plates) aligned ^{15}N-Gly_2, ^{15}N-Ala_3 gramicidin A (gA) in hydrated dimyristoylphosphatidylcholine (DMPC) recorded using the HHCP and ADCP schemes. GA is a polypeptide of 15 amino acid residues having the sequence of formyl-L-Val_1-Gly_2-L-Ala_3-D-Leu_4-L-Ala_5-D-Val_6-L-Val_7-D-Val_8-L-Trp_9-D-Leu_{10}-L-Trp_{11}-D-Leu_{12}-LTrp_{13}-D-Leu_{14}-L-Trp_{15}-ethanolamine, whose high-resolution structure in lipid bilayers has been uniquely defined using 120 orientational restraints from solid-state oriented sample NMR [30]. The signals at 136 and 222 ppm are the anisotropic chemical shift resonances from the ^{15}N-Gly_2 and ^{15}N-Ala_3 sites, respectively. As shown in Fig. S6, the obtained T_{1d} values were only 1.23 ± 0.25 and 1.24 ± 0.14 ms for the resonances at 136 and 222 ppm, respectively. Such short T_{1d} values make the polarization transfer through DOCP practically insufficient. Nevertheless, the ADCP scheme using adiabatically demagnetizing the ^{1}H magnetization not only improves the signal intensities by ~50% (c.f., Fig. 6a) but also significantly broadens the matching bandwidth over the HHCP scheme with spin-locking the ^{1}H magnetization (Fig. 6b versus 6c).

Fig. 7a shows the ^{13}C CPMAS spectra of the alanine powder sample spinning at 17 kHz using different CP schemes with the CP contact time of 1 and 3 ms. In our RACP experiments, the ^{1}H RF amplitude was kept constant while the ^{13}C RF amplitude was ramped from 100% down to 70%. At $\tau_{CP} = 1$ ms, RACP and ADCP give rise to roughly the same signal intensities for the CH (at 51.8 ppm) and CH_3 (at 22.5 ppm) resonances, about 60% and 100% more signals as compared to the HHCP. While RACP results in about 60% more signal intensity for the non-protonated COO resonance at 178.5 ppm than the HHCP and ADCP. However, when $\tau_{CP} = 3$ ms, ADCP has the highest signal intensities for all three resonances over HHCP (about 150%, 176%, and 354% for the COO, CH, and CH_3 signals, respectively) and RACP (about 35%, 30%, and 31% for the COO, CH, and CH_3 signals, respectively). Fig. 7b shows the CP matching profiles for these three schemes. For HHCP, the CP matching sidebands are observed, as being observed in the literature [5,6]. For both RACP and ADCP, the CP matching condition is significantly broadened, as compared to HHCP.

For both HHCP and RACP, the ^{1}H is spin-locked during the CP transfer. As a result, their CP dynamics are subject to ^{1}H $T_{1\rho}$. As indicated in Fig. 7c, the ^{1}H $T_{1\rho}$ is relatively short for the alanine sample, such that the CH and CH_3 signals decay at $\tau_{CP} < 1$ ms and the non-protonated COO signal starts to decay before it could be fully polarized. While for the ADCP, the ^{1}H RF amplitude ramps down linearly, thus it is not subject to the ^{1}H magnetization decay at any given spin-lock field. As indicated in Fig. 7c, the polarized ^{13}C signals decay a lot slower in the ADCP experiments than in the HHCP and RACP experiments. In order to compare the CP dynamics under RACP and ADCP, we used $T_{1\rho}{}^{H}$ for characterizing the ^{1}H decay and T_{CH} for the CP transfer time. Therefore, their CP dynamics can be fitted using this classical model [9]:

$$M(\tau_{CP}) = M_0 \left[\exp\left(-\frac{\tau_{CP}}{T_{1\rho}{}^{H}} \right) - \exp\left(-\frac{\tau_{CP}}{T_{CH}} \right) \right] \Big/ \left(1 - \frac{T_{CH}}{T_{1\rho}{}^{H}} \right). \tag{10}$$

Here, M_0 represents the equilibrium magnetization. The fitting results are listed in Table 1. Clearly, the $T_{1\rho}{}^{H}$ values are almost doubled for CH_3 and CH and about tripled for COO when using ADCP than RACP. Although ADCP also lengthens their CP transfer times, it polarizes more signals over RACP, especially for the non-protonated resonances such as COO.

It is known that, under MAS, the dipolar coupling d_{IS} becomes time-dependent and the non-zero coefficients appear at $\pm n\omega_r$, where $n = 1$ and 2. Accordingly, the HHCP matching condition is broken up into a series of sidebands at $\omega_{1I} = \omega_{1S} \pm n\omega_r$ [5,6]. Analogically, for ADCP under MAS, Δ and Σ in the zero- and double-quantum subspaces also break up into a series of CP matching sidebands as $\Delta(t) = \omega_{1I}(t) - \omega_{1S} \pm n\omega_r$ and $\Sigma(t) = \omega_{1I}(t) + \omega_{1S} \pm n\omega_r$. Under the slow and moderate spinning rates, i.e., ω_r is less than the homo- and hetero-nuclear dipolar couplings, the CP dynamics resemble the static case and thus the ADCP experiments are robust, as demonstrated in Fig. 7. However, at fast MAS, the adiabatic sweep of $\omega_{1I}(t)$ should be carefully chosen to ensure that only one of the CP matching sidebands is used for CP transfer in either zero- or double-quantum subspaces, as discussed by Hediger et al. [22].

5. Conclusions

It has been demonstrated that the efficient cross polarization from ^{1}H to the *S* spin can be achieved by adiabatically demagnetizing ^{1}H while applying a constant RF amplitude on the *S* spin. This new adiabatic demagnetization cross polarization (ADCP) scheme utilizes the adiabatic passage for effective polarization transfer from ^{1}H to the *S* spin. It has an extremely broad CP matching bandwidth especially in the static experiments, owing to the fact that the adiabatic passage

condition can be fulfilled at different positions during the CP contact time as the ^{1}H RF amplitude is linearly decreased. More importantly, the dipolar ordered state generated during the ^{1}H demagnetization could be converted into the *S* polarization, further enhancing the signals, in the systems where the lifetime of the dipolar ordered state is long. Moreover, ADCP can allow for a much weaker RF amplitude being applied on the *S* spin to achieve the optimal cross-polarization, which is very useful in the experiments using mechanically/magnetically aligned biological samples [31] where a large rectangular coil is typically used for better sensitivity. As in the magic-angle-spinning (MAS) experiments, ADCP appears to have a much slower ^{1}H decay in the spin dynamics using the classical model, especially for the non-protonated sites such as COO, as compared to those schemes where the ^{1}H magnetization is spin-locked at a given RF amplitude. Although it is not clear what the physical meaning of the ^{1}H decay is during the ^{1}H demagnetization, the ability of lengthening the ^{1}H decay during cross polarization, as in the spin-locking along the magic angle [27], could greatly enhance the polarized signals, toward quantitative measurements in solid-state CPMAS NMR.

CRediT authorship contribution statement

Yucheng Li: Going through intense literature search, theoretical analyses, contributed to manuscript writing. **Shengyu Zhang:** Going through intense literature search, theoretical analyses, contributed to manuscript writing. **Ze Wu:** Theoretical analyses, contributed to manuscript writing. **Xinhua Peng:** Oversighting the project, conceptualization, theoretical analyses, writing manuscript. **Riqiang Fu:** Oversighting the project, conceptualization, designing and implementing experiments, analyzing data, writing initial draft.

Declaration of competing interest

The authors declare that they have no known competing financial interests or personal relationships that could have appeared to influence the work reported in this paper.

Acknowledgement

All NMR experiments were carried out at the National High Magnetic Field Lab (NHMFL) supported by the NSF Cooperative Agreement DMR-1644779 and the State of Florida. X.H.P. acknowledges the supports from the National Key R&D Program of China (Grants No. 2018YFA0306600), the National Science Foundation of China (Grants No. 11927811, 12150014), and Anhui Initiative in Quantum Information Technologies (Grant No. AHY050000).

Appendix A. Supplementary data

Supplementary data to this article can be found online at https://doi.org/10.1016/j.mrl.2022.07.001, which include: plots of $C_I(t)$ and $C_S(t)$ within the contact time, CP matching profiles under different CP schemes in static samples, the lifetime measurements of the dipolar ordered states, AD/DO-CP spectra at different experimental conditions, buildups of the ^{15}N signals during the contact time in the ADCP experiments.

References

[1] A. Pines, M.G. Gibby, J.S. Waugh, Proton-enhanced NMR of dilute spins in solids, J. Chem. Phys. 59 (1973) 569–590.
[2] S.R. Hartmann, E.L. Hahn, Nuclear double resonance in rotating frame, Phys. Rev. 128 (1962) 2042–2053.
[3] C.P. Slichter, W.C. Holton, Adiabatic demagnetization in a rotating reference system, Phys. Rev. 122 (1961) 1701–1708.
[4] A.G. Anderson, S.R. Hartmann, Nuclear magnetic resonance in the demagnetized state, Phys. Rev. 128 (1962) 2023–2041.
[5] E.O. Stejskal, J. Schaefer, J.S. Waugh, Magic-angle spinning and polarization transfer in proton-enhanced NMR, J. Magn. Reson. 28 (1977) 105–112.
[6] M. Sardashti, G.E. Maciel, Effects of sample spinning on cross polarization, J. Magn. Reson. 72 (1987) 467.
[7] D.A. McArthur, E.L. Hahn, Rotating-frame nuclear-double-resonance dynamics: dipolar fluctuation spectrum in CaF_2, PR 188 (1969) 609–638.
[8] D.E. Demco, J. Tegenfeldt, J.S. Waugh, Dynamics of cross polarization in nuclear magnetic double resonance, Phys. Rev. B 11 (1975) 4133–4151.
[9] M. Mehring, Principles of High Resolution NMR in Solids, second ed., Springer-Verlag, New York, 1983.
[10] W. Kolodziejski, J. Klinowski, Kinetics of cross-polarization in solid-state NMR: a guide for chemists, Chem. Rev. 102 (2002) 613–628.
[11] C. Fuelber, D.E. Demco, B. Bluemich, The influence of molecular motion on cross polarization in cross-linked elastomers, Solid State Nucl. Magn. Reson. 6 (1996) 213–223.
[12] M.H. Levitt, D. Suter, R.R. Ernst, Spin dynamics and thermodynamics in solid-state NMR cross polarization, J. Chem. Phys. 84 (1986) 4243–4255.
[13] S. Hediger, B.H. Meier, N.D. Kurur, G. Bodenhausen, R.R. Ernst, NMR cross polarization by adiabatic passage through the Hartmann hahn condition (APHH), Chem. Phys. Lett. 223 (1994) 283–288.
[14] E. Chiarparin, P. Pelupessy, G. Bodenhausen, Selective cross-polarization in solution state NMR, Mol. Phys. 95 (1998) 759–767.
[15] S. Zhang, Quasi-adiabatic polarization transfer in solid-state NMR, J. Magn. Reson. 110 (1994) 73–76.
[16] H. Kim, T.A. Cross, R. Fu, Cross-polarization schemes for peptide samples oriented in hydrated phospholipid bilayers, J. Magn. Reson. 168 (2004) 147–152.
[17] K.J. Harris, A. Lupulescu, B.E.G. Lucier, L. Frydman, R.W. Schurko, Boradband adiabatic inversion pulses for cross polarization in wideline solid-state NMR spectroscopy, J. Magn. Reson. 224 (2012) 38–47.
[18] T.M. Barbara, E.H. Williams, Modulated sequences for cross polarization during high-speed MAS, J. Magn. Reson. 99 (1992) 439.

[19] X. Wu, K.W. Zilm, Cross polarizaton with high-speed magic-angle spinning, J. Magn. Reson. 104 (1993) 154.
[20] S. Hediger, B.H. Meier, R.R. Ernst, Cross Polarization under fast magic angle sample spinning using amplitude-modulated spin-lock sequencs, Chem. Phys. Lett. 213 (1993) 627–635.
[21] S. Hediger, B.H. Meier, R.R. Ernst, Rotor-synchronized amplitude-modulated nuclear magnetic resonance spin-lock sequences for improved cross polarization under fast magic angle sample spinning, J. Chem. Phys. 102 (1995) 4000–4011.
[22] S. Hediger, B.H. Meier, R.R. Ernst, Adiabatic passage Hertmann-Hahn cross polarization in NMR under magic angle spinning, Chem. Phys. Lett. 240 (1995) 449–456.
[23] O.B. Peersen, X. Wu, I. Kustanovich, S.O. Smith, Variable-amplitude cross polarization MAS NMR, J. Magn. Reson. 104 (1993) 334–339.
[24] G. Metz, X. Wu, S.O. Smith, Ramped-amplitude cross polarization in magic-angle-spinning NMR, J. Magn. Reson. 110 (1994) 219–227.
[25] A.C. Kolbert, A. Bielecki, Broadband hartmann-hahn matching in magic-angle spinning NMR via an adiabatic frequency sweep, J. Magn. Reson. 116 (1995) 29–35.
[26] R. Fu, P. Pelupessy, G. Bodenhausen, Frequency-modulated cross-polarization for fast magic angle spinning NMR at high field: relaxing the Hartmann-Hahn condition, Chem. Phys. Lett. 264 (1997) 63–69.
[27] R. Fu, J. Hu, T.A. Cross, Towards quantitative measurements in solid-state CPMAS NMR: a Lee-Goldburg frequency modulated cross-polarization scheme, J. Magn. Reson. 168 (2004) 8–17.
[28] R. Fu, Efficient heteronuclear dipolar decoupling in NMR of static solid samples using phase-wiggled two-pulse phase modulation, Chem. Phys. Lett. 483 (2009) 147–153.
[29] B.M. Fung, A.K. Khitrin, K. Ermolaev, Am improved broadband decoupling sequence for liquid crystals and solids, JMR (J. Mol. Recognit.) 142 (2000) 97–101.
[30] R.R. Ketchem, W. Hu, T.A. Cross, High-resolution conformation of gramicidin-a in a lipid bilayer by solid-state NMR, Science 261 (1993) 1457–1460.
[31] R. Fu, W.W. Brey, T.A. Cross, Aligned membrane proteins: structural studies, in: A.E. McDermott, T. Polenova (Eds.), Encyclopedia of Magnetic Resonance, Johm Wiley & Sons Ltd, Chichester, UK, 2010, pp. 417–432.

Yuchen Li received the B.S. degree in applied physics from the School of Physics and Electronics, CSU, Changsha in 2018. Currently, he is pursuing the Ph.D. degree in the School of Physical Science, USTC, Hefei. His research interests include quantum control, quantum simulation and quantum metrology using solid-state NMR system.

Shengyu Zhang received the B.S. degree in physics from the School of Physics and Technology, WHU, Wuhan in 2020. Currently, he is pursuing the Ph.D. degree in the School of Physical Science, USTC, Hefei. His research interests include quantum control, quantum simulation and quantum metrology using solid-state NMR system.

Ze Wu received the B.S. degree in theoretical physics from the School of Physics Sciences, USTC, Hefei in 2016. Currently, he is pursuing the Ph.D. degree in the School of Physical Science, USTC, Hefei. His research interests include quantum control, quantum simulation and open quantum systems.

Xinhua Peng received her Ph.D. degree in Atomic and Molecular Physics from Wuhan Institute of Physics and Mathematics, Wuhan in 2003. She is currently a professor in the School of Physical Science, USTC, Hefei. Her major research interests focus on quantum information processing using magnetic resonance technology.

Riqiang Fu received his B.S. degree in Electrical Engineering from University of Science and Technology of China (USTC) in 1986 and his PhD degree in 1992 with Prof. Chaohui Ye at Wuhan Institute of Physics. Currently he is a Research Faculty III at National High Magnetic Field Lab. He specializes in solid-state NMR methodology development and NMR applications in materials science and biological systems.